



Research article

In situ growth of BiOBr on copper foam conductive substrate with enhanced photocatalytic performance

Ying Liang^{a,1}, Ting Yu^{a,1}, Man Lang^a, Fengjie Chen^{a,*}, Mengxi Cao^a, Bolei Chen^a, Pu Wang^a, Yong Liang^a, Yawei Wang^{a,b}

^a Hubei Key Laboratory of Environmental and Health Effects of Persistent Toxic Substances, School of Environment and Health, Jiangnan University, Wuhan, 430056, China

^b State Key Laboratory of Environmental Chemistry and Eco-toxicology, Research Center for Eco-environmental Sciences, Chinese Academy of Sciences, Beijing, 100085, China

ARTICLE INFO

Keywords:

Surface modified
Functional photocatalyst
BiOBr/Cu foam
Charge separation
Methylene blue degradation

ABSTRACT

Photocatalysis technology based on solar-powered semiconductors is widely recognized as a promising approach for achieving eco-friendly, secure, and sustainable degradation of organic contaminants. Nevertheless, conventional photocatalysts exhibit drawbacks such as a wide bandgap, and rapid recombination of photoinduced electron/hole pairs, in addition to complicated separation and recovery procedures. In this research, we cultivated BiOBr in situ on the surface of copper foam to fabricate a functional photocatalyst (denoted as BiOBr/Cu foam), which was subsequently employed for the photodegradation of Methylene Blue. Based on photodegradation experiments, the 0.3 BiOBr/Cu foam demonstrates superior photocatalytic efficacy compared to other photocatalysts under solar light irradiation. Furthermore, its ease of separation from the solution enhances its potential for reuse. The analysis of charge transfer revealed that the copper foam functions as an effective electron scavenger within the BiOBr/Cu foam, thereby facilitating charge separation and the generation of photo-induced holes. This phenomenon contributes to a significantly enhanced production of hydroxyl radicals. This study provides a valuable perspective on the design and synthesis of photocatalysts with heightened practicality, employing a conductive substrate.

1. Introduction

Photocatalysis technology, relying on solar-powered semiconductors, is widely acknowledged as a promising strategy for achieving eco-friendly, secure, and sustainable degradation of organic contaminants. This recognition is attributed to its notable advantages, which include remarkable efficiency, cost-effectiveness, energy conservation, stability, and the absence of secondary pollution [1,2]. The basic principle of semiconductor photocatalysis technology is that the semiconductor photocatalyst after being photoexcited, the photo-electrons jump to the conduction band from the valence band and form photo-holes in the valence band [3]. The prompt interaction of photo-generated electrons and holes with O_2 , H_2O , or OH^- leads to the formation of reactive oxygen species (ROS), comprising superoxide anion radicals ($\bullet O_2^-$) and hydroxyl radicals ($\bullet OH$) [4], which degrade pollutants in the environment.

* Corresponding author.

E-mail address: fjiechen@jhun.edu.cn (F. Chen).

¹ These authors contributed equally to this work and should be considered co-first authors.

<https://doi.org/10.1016/j.heliyon.2024.e25929>

Received 24 October 2023; Received in revised form 26 January 2024; Accepted 5 February 2024

Available online 17 February 2024

2405-8440/Â© 2024 The Authors. Published by Elsevier Ltd. This is an open access article under the CC BY-NC-ND license (<http://creativecommons.org/licenses/by-nc-nd/4.0/>).

Nevertheless, widely employed semiconductor photocatalysts, such as TiO_2 , $\text{g-C}_3\text{N}_4$, ZnO , etc., are burdened by three notable drawbacks [5]. The first challenge is the wide band gap, leading to diminished responsiveness to visible light. The second challenge involves the rapid photo-induced recombination of electron/hole pairs, resulting in a diminished quantum yield. The final obstacle is the intricate separation and recovery processes, contributing to additional processing costs [6,7]. Therefore, it has become an important research direction on the development and production of innovative visible-light-driven photocatalysts that possess practical utility.

Bismuth oxobromide (BiOBr) has been drawing more focus from researchers due to its cost-effectiveness and toxicity, appropriate band gap energy, and superior chemical stability [8]. However, the common drawbacks of semiconductor photocatalysts also are the main issues that may limit the performance of BiOBr in the photodegradation process [9]. Recent studies have proposed a solution, that is, conductive substrates such as Cu foam, Ni foam, metal wire meshes, and carbon nanotube films as a substrate to cooperate with nano-photocatalysts [10]. On the one hand, the conductive substrates can immobilize the photocatalysts. The immobilized photocatalysts have the capacity for separation and recurrent utilization in the photodegradation process through an uncomplicated washing step. On the other hand, the combination with a conductive substrate can decrease the photocatalyst's band gap, promote the visible light response, and accelerate the photoexcited electron/hole separation inside the photocatalyst.

Copper (Cu) foam, a novel multifunctional material characterized by an abundance of interconnected or isolated pores, has attracted significant attention due to its cost-effectiveness, ease of manufacturing, and environmentally friendly attributes [11]. As a catalyst conductive substrate, it can not only promote the photocatalytic performance of the catalyst and speed up the photodegradation reaction rate but also improve the separation and reuse process of the photocatalyst to reduce the cost of wastewater treatment. A study by Ji reported that dendritic ZnO/CuO nanoparticles attached to Cu foam enhanced the visible light response and inhibited photoexcited electron/hole complexation, resulting in rapid degradation of RhB [12]. Based on these findings, a reasonable guess is growing BiOBr on Cu foam can overcome the common drawback of photocatalysts, and achieve effective degradation of organic pollutants.

In this study, growing BiOBr in situ on copper (Cu) foam to achieve effective degradation of organic pollutants. Methylene blue (MB) represents organic pollutants to evaluate the photodegradation performance of different BiOBr doses on Cu foam. The mechanism of ROS generation and MB photodegradation was studied by ROS assay and electrochemical experiment. This work is expected to deliver a perspective on the design and fabrication of photocatalysts with high practicability.

2. Materials and methods

2.1. Chemicals and materials

All chemicals utilized in this study were of analytical grade, including hydrochloric acid (HCl, CAS: 7647-01-0), ethylene glycol ($\text{C}_2\text{H}_6\text{O}_2$, CAS: 107-21-1), Hexadecyl trimethyl ammonium bromide (CTAB, CAS: 57-09-0), sodium hydroxide (NaOH, CAS:1310-73-2), Isopropanol (IPA, CAS: 67-63-0), Potassium bromate (KBrO_3 , CAS: 7758-01-2), Polyvinylpyrrolidone (PVP, CAS: 9003-39-8), Sodium oxalate ($\text{Na}_2\text{C}_2\text{O}_4$, CAS: 62-76-0), Bismuth nitrate ($\text{Bi}(\text{NO}_3)_3$, CAS: 10361-44-1), Acetone ($\text{C}_3\text{H}_6\text{O}$, CAS: 67-64-1), Ethanol ($\text{C}_2\text{H}_6\text{O}$, CAS: 64-17-5), p-benzoquinone ($\text{C}_6\text{H}_4\text{O}_2$, CAS: 106-51-4), Methylene Blue (MB, CAS: 61-73-4), Sodium oxalate (CAS: 62-76-0). The Cu foam was obtained from Kunshan Lanfeng New Material Co., LTD.

2.2. Synthesis of BiOBr

BiOBr was synthesized as follows: 0.1 mol/L $\text{Bi}(\text{NO}_3)_3 \cdot 5\text{H}_2\text{O}$ and 0.1 mol/L CTAB were added to a blended solution of 70 mL ethylene glycol and 10 mL deionized through ultrasonic dissolution water for 10 min. Afterward, transferred the blended solution to the stainless steel reactor polytetrafluoroethylene lining, and a hydrothermal treatment was conducted at 160°C for 4 h. Subsequently, the resulting precipitation subjected to three washes with deionized water and ethanol, respectively, followed by centrifuged for 5 min at 5000 rpm. Finally, the resulting precipitation is dried for 6 h at 60°C .

2.3. Synthesis of BiOBr/Cu foam

BiOBr/Cu foam was synthesized on a Cu foam substrate (40 mm \times 75 mm) by hydrothermal method [13] (Fig. S1). The cleaning method of Cu foam is to soak in 0.1 mol/L HCl followed by ultrasonication for 2 min, then soak in water, acetone, and ethanol respectively, and ultrasonication treatment 5 min, and 60°C drying 6 h. 0.1 mol/L $\text{Bi}(\text{NO}_3)_3 \cdot 5\text{H}_2\text{O}$ and 0.1 mol/L CTAB in a mixture of 70 mL $\text{C}_2\text{H}_6\text{O}_2$ and 10 mL deionized water were dissolved by sonication for 10 min. Next, 0 mg, 100 mg, and 200 mg polyvinylpyrrolidone were added to the solution respectively. Then, hydrothermal treatment is carried out under the same conditions as BiOBr. The precipitate obtained subjected to three washes with deionized water and ethanol followed by drying for 6 h at 60°C . According to the amount of polyvinylpyrrolidone added, the amount of BiOBr in-situ grown on the Cu foam was 0.11 g/g, 0.19 g/g, and 0.30 g/g determined by thermogravimetric analysis (Table S1), respectively, so it was named 0.1 BiOBr/Cu foam, 0.2 BiOBr/Cu foam, and 0.3 BiOBr/Cu foam.

2.4. Morpho-structural characterization of BiOBr and BiOBr/Cu foam

The morphologies of BiOBr and BiOBr/Cu were explored using field emission scanning electron microscopy (FESEM, TESCAN MIRA LMS, Czech). The surface chemical groups were using an X-ray photoelectron spectroscopy (XPS, ESCALAB 250X, America). The

crystal structure was examined using an X-ray diffractometer (XRD, X'Pert PRO MPD, Netherlands). The XRD analysis covered a 2 θ scanning range from 5° C to 90° C, and the scanning speed was set at 2°/min. The diffuse reflectance UV-visible absorption spectra of each sample were measured using a UV-Vis spectrometer (Lambda 25, America) at ambient temperature. Additionally, photoluminescence was assessed using a steady-state transient fluorescence spectrometer (Edinburgh FLS1000, England) with a 320 nm He-Cd excitation laser source. The maximum absorbance of methylene blue was measured at 463 nm by UV-vis spectrophotometer (TU-1810D, China). The assessment of photocurrent and electrochemical impedance spectroscopy (EIS) measurements was carried out utilizing a conventional three-electrode system integrated into an electrochemical analyzer (CHI760E, China). This system included a coiled Pt wire serving as the working electrode, along with an Ag/AgCl electrode employed as the counter and reference electrodes. The water circulation system used in this study is a circulating water-cooling unit (RC-2 lite, Germany), and the light source used is xenon lamp (Beijing Perfectlight MICROSOLAR 300, 120 mW/cm²).

2.5. Photodegradation experiments

20 mm × 20 mm of BiOBr/Cu was added to 50 mL of 10 mg/L MB solution in a glass reactor. To ensure the consistency of temperature, the RC-2 lite circulating water-cooling unit was used to cool the glass reactor. Allowing the mixed solution to stand in darkness for a duration of 15 min to attain adsorption/desorption equilibrium. Then, the supernatant was taken 2 mL every 10 min under sunlight irradiation. The absorbance was measured with an ultraviolet spectrophotometer at 463 nm. Finally, the concentration and degradation rate of the MB solution at different times were calculated according to the change in absorbance.

2.6. ROS experiment

The mechanism of photodegradation of MB was investigated by active species capture experiment. During the photocatalytic reaction, the quenching agents of different active species were added, and the effect of each active species was judged by the inhibiting or promoting effect of the quenching agents on the photocatalytic reaction. 3 mmol/L isopropanol, p-benzoquinone, sodium oxalate, and potassium bromate were added to the solution as quenchers of •OH, superoxide anion radical, photoelectrons, and holes, respectively. The ESR measurements were conducted employing a Bruker A300-10/12 instrument, with the detection of •OH achieved using a 50 mM 5,5-Dimethyl-1-pyrroline N-oxide. Other experimental conditions are the same as photodegradation experiments.

3. Result and discussion

3.1. BiOBr/Cu foam characterization

The XRD spectra for Cu foam, BiOBr, and BiOBr/Cu foam photocatalysts are displayed in Fig. 1a. Unique peaks of diffraction located at 33°, 44°, 47°, 51°, and 75° are both found in the BiOBr/Cu foam. Additionally, peaks at 33° and 47° are the characteristic peaks of BiOBr (PDF#09-0393). The characteristic diffraction peaks at 44°, 51°, and 75° could be attributed to Cu (PDF#04-0836). To further explore the impact of the loading procedure on the crystal structure of Cu/BiOBr, the equation was employed to compute the crystallite size D : $D = \frac{K\lambda}{\beta \cos \theta}$, where K is Scherrer's constant, β is the full width at half-maximum, λ is wavelength, and θ is the peak position, and the outcome was shown in Table S2. The crystallite size of BiOBr decreased from 21.82 nm to 12.02 nm after loading. The small crystal size is the main cause of the observed broadening of X-ray peaks with higher loadings of BiOBr [14,15]. These results

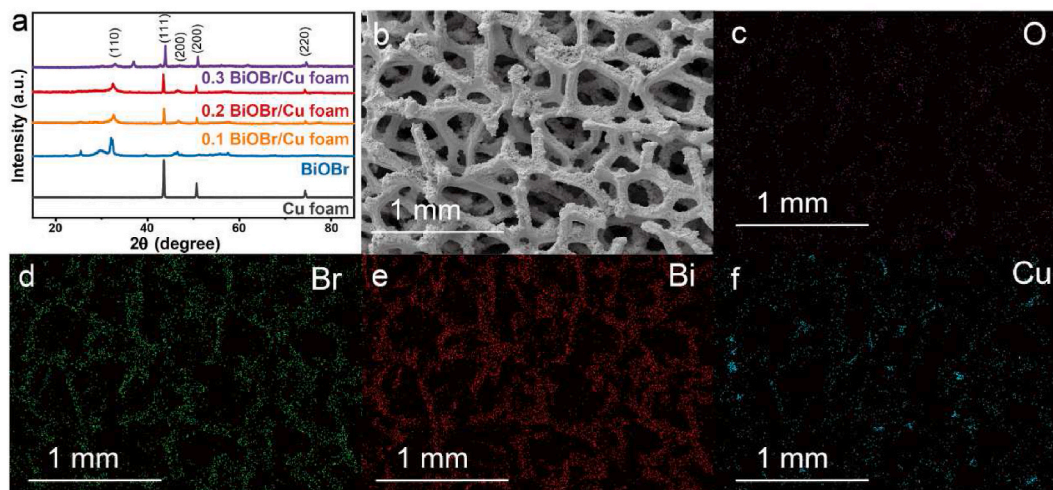


Fig. 1. XRD patterns of Cu foam, BiOBr, 0.1 BiOBr/Cu foam, 0.2 BiOBr/Cu foam, and 0.3 BiOBr/Cu foam (a); SEM images (b), and EDS element maps of (c) O, (d) Br (e) Bi and (f) Cu in BiOBr/Cu foam.

show that BiOBr was successfully loaded on Cu foam. For further verification, optical photographs and SEM measurements have been performed on the BiOBr/Cu foam samples. The optical photograph clearly shows a layer of particles on the surface of the Cu foam (Fig. S2). In accordance with the SEM image, well-ordered reticulate structures with smooth surfaces and flower-like structures were found in the Cu foam and BiOBr (Figs. S3a and b). After adding the $\text{Bi}(\text{NO}_3)_3$ and CATB solution in Cu foam, the flower-like structure appeared on the surface of Cu foam in the BiOBr/Cu foam samples (Fig. 1b). In addition, as expected, BiOBr/Cu foam contained Cu, Bi, O, and Br elements (Fig. S4). And according to EDS, with the increase of BiOBr load, the atomic proportion of Br increases from 12.590% of 0.1 BiOBr/Cu foam to 17.446% of 0.2 BiOBr/Cu foam and finally to 20.646% of 0.3 BiOBr/Cu foam. The trend in the atomic proportion of Bi also corresponds to that of Br, with a gradual increase from 7.352% at 0.1 BiOBr/Cu foam to 14.324% at 0.3 BiOBr/Cu foam (Table S3). Moreover, the peak height of Cu in the EDS spectra decreased gradually as the loading of BiOBr increased (Fig. S5). According to the elemental mapping results, the elements O, Br, Bi and Cu exhibited a homogeneous distribution across the particles (Fig. 1c-f). These findings also implied that BiOBr was successfully synthesized on the Cu foam surface.

The surface properties of photocatalyst were investigated according to the results of nitrogen adsorption isotherm. Fig. S6 shows the nitrogen adsorption isotherm curve of Cu foam, BiOBr, BiOBr/Cu foam samples. A type IV isotherm is exhibited in all curves with a distinct hysteresis loops, a characteristic feature of mesoporous structures [16]. The Brunauer-Emmett-Teller (BET) surface areas, pore volumes, and Barrett-Joyner-Halenda (BJH) pore diameters have been provided in Table S4 [17]. The BET surface area of BiOBr, Cu foam, 0.1 BiOBr/Cu foam, 0.2 BiOBr/Cu foam, 0.3 BiOBr/Cu foam is 1.09, 5.11, 0.93, 7.20, 12.84 m^2/g . Notably, the 0.3 BiOBr/Cu foam has a higher BET surface area and pore volume than 0.1 BiOBr/Cu foam and 0.2 BiOBr/Cu foam. At the same time, 0.3 BiOBr/Cu foam exhibits a greater pore volume (0.0194 cm^3/g), in contrast to 0.1 BiOBr/Cu foam (0.0027 cm^3/g) and 0.2 BiOBr/Cu foam (0.0136 cm^3/g). The introduction of BiOBr resulted in an increase in the material's specific surface area and pore volume, signifying an expanded contact area between the material and the reactants. Consequently, this enhancement led to the availability of more active sites, thereby promoting the reaction [18]. Moreover, the gradual reduction in pore diameter can be attributed to the heightened presence of crosslinking points with higher BiOBr loading [19]. The characterization of functional groups in the samples was performed using XPS. Analysis of BiOBr/Cu foam revealed the presence of elements Br, O, Bi, and Cu (Fig. S7). The Bi 4f spectrum (Fig. 2a) separates into Bi 4f_{5/2} and Bi 4f_{7/2} tracks at 163.8 eV and 158.5 eV, which indicated the presence of Bi³⁺ within the BiOBr [20]. Two discernible peaks are observed in the Br 3d spectrum (Fig. 2b), with positions of 68.9 eV and 67.7 eV, corresponding to Br 3d_{2/3} and Br 3d_{5/2}, respectively. These observations suggest the existence of Br⁻ in the BiOBr/Cu foam [21]. The Cu 2p spectrum (Fig. 2c) is Cu 2p_{3/2} peak, that separates into 932.6 eV and 934.6 eV, related to Cu₂O or Cu and CuO respectively [22]. Compared with BiOBr and Cu foam, Bi 4f and Cu 2p in BiOBr/Cu foam exhibit a slight chemical redshift and blueshift. This is probably because the intimate interaction between BiOBr and Cu foam might also affect the displacement of Bi 4f and Cu 2p peaks and could offer a potential route for the migration and separation of charges. In Fig. 2d, three definite O 1s peaks are observed at 529.5 eV, 530.9 eV and 532.0 eV, which are derived from the lattice O atoms (Bi-O and Cu-O bonds) and surface adsorbed H₂O or other oxygen-containing groups, respectively [23]. These findings reaffirm the successful synthesis of composites of BiOBr/Cu foam.

Fig. 3 displays the visible light response of the BiOBr/Cu foam photocatalysts with UV-Vis DRS. BiOBr has an absorption edge of 450 nm, indicating bare BiOBr hardly absorbed visible light. Conversely, both Cu foam, BiOBr/Cu foam exhibited an extensive spectrum of visible light absorption, extending as far as 780 nm (Fig. 3a), implying the potential for a visible light response facilitated by a conductive substrate [24]. This is consistent with previous research [25]. Furthermore, the optical absorption in proximity to the

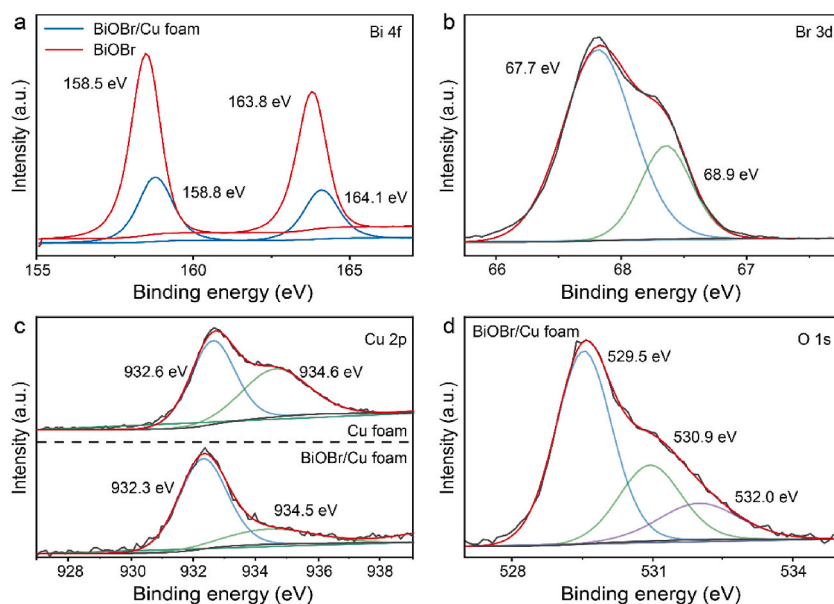


Fig. 2. XPS spectra of BiOBr/Cu foam: (a) Bi 4f; (b) Br 3d; (c) Cu 2p; and (d) O 1s.

band edge adheres to the formula: $ah\nu = A(h\nu - E_g)^{n/2}$, where a , ν , A and E_g are the absorption coefficient, the bandgap energy and a constant, the light frequency, respectively [26]. The intercepts to the x-axis give a reliable estimate of the sample band gap energy, as shown in Fig. 3b. The estimated E_g values of BiOBr, Cu foam, 0.1 BiOBr/Cu foam, 0.2 BiOBr/Cu foam, and 0.3 BiOBr/Cu foam are about 2.95 eV, 2.04 eV, 2.04 eV, 2.59 eV, and 2.80 eV respectively, indicating BiOBr load on Cu foam would increase the band gap of Cu foam, resulting in a higher charges separation efficiency.

3.2. The photocatalytic properties of BiOBr/Cu foam

Photocatalytic properties of BiOBr/Cu foams were investigated under solar radiation using 10 mg/L Methylene Blue (MB) as a photodegradation agent. As shown in Fig. 4a, 22.5% of MB was removed after 100 min solar light irradiation in the case of no catalyst. This phenomenon may be attributed to its inherent degradation through photolysis [27]. In the presence of Cu foam, the photocatalytic degradation rate of Methylene Blue (MB) did not deviate significantly from the case without a catalyst, suggesting a lack of photocatalytic activity in Cu foam. Conversely, the presence of BiOBr led to a large amount of photodegradation of MB. Notably, through the modification of BiOBr onto the Cu foam, the photocatalytic activities of BiOBr/Cu foam become much better than that of the pristine BiOBr. Photodegradation of MB by 0.3 BiOBr/Cu foam (98.9%) was significantly greater than that by 0.1 BiOBr/Cu foam (45.6%) and 0.2 BiOBr/Cu foam (52.4%), which indicated that 0.3 BiOBr/Cu foam exhibited superior photocatalytic properties. For further quantitative investigation using pseudo-first-order reaction: $\ln(c/c_0) = -kt$, where k is the rate constant for the pseudo-first-order reaction, c and c_0 is the MB concentrations at a specified time and the initial time, t is the reaction time of the photodegradation process [28]. The observable rate of MB photodegradation in the catalyst existence was qualified in Fig. 4b. The value of k and correlation coefficient (R^2) are shown in Table S5. The k value of Cu foam, BiOBr, 0.1 BiOBr/Cu foam, 0.2 BiOBr/Cu foam, and 0.3 BiOBr/Cu foam was 0.0026, 0.0031, 0.0058, 0.0070, and 0.0175, respectively, corroborating that 0.3 BiOBr/Cu foam has the highest efficiency of photodegradation among other samples.

The pH was a key factor affecting the efficiency of the photodegradation process [29]. This is because the concentration of hydrogen and hydroxyl ions (H^+ and OH^-) can affect the ROS generation, and then affect the photodegradation of organic pollutants [30]. The effect of pH on the photodegradation of Methylene Blue (MB) by 0.3 BiOBr/Cu foam was investigated under solar light irradiation, using initial MB concentrations of 10 mg/L. The results are presented in Fig. 4c. With an increase in pH within the range of 3.02–11.00, there was a corresponding increase in the rate of MB degradation. This phenomenon may be attributed to the amount of $\bullet OH$ produced increases with the increase of OH^- concentration in the solution [31], resulting in a higher photodegradation efficiency of MB.

Stability is likewise a crucial aspect when assessing the photocatalytic performance of photocatalysts. To investigate the stability of the 0.3 BiOBr/Cu, a photodegradation cycle of MB was run under solar irradiation. As depicted in Fig. 4d, the photodegradation rate of MB was maintained at 90.5% after 4 cycles of solar irradiation. In addition, we compared the XRD before and after the photocatalytic material degraded MB, and found that the composition of the photocatalyst did not change significantly, which proved the stability of the material (Fig. S8).

Based on the aforementioned discussion, Photodegradation time and photodegradation efficiency of 0.3 BiOBr/Cu foam were 100 min and 98.9%, respectively, which were superior to the $Zn_3(BTC)_2$ (420 min and 50%) [32], Cu-L photocatalyst (150 min and 84.22%) [33], TiO_2/CS 4:1 (120 min and 94.09%) [34], PVDF/GO/ZnO (100 min and 86.84%) [35], and ZnO nanorods (180 min and 60%) [36] (Table S6). Thus, the results showed that the 0.3 BiOBr/Cu foam exhibited outstanding photocatalytic efficacy.

3.3. Charge transfer of BiOBr/Cu foam

The quantum yield of photocatalysts under light irradiation is determined by the efficiency of charge separation [37]. As far as we all know, metals always act as electron scavengers in the composite photocatalyst [38]. Thus, the charge separation was facilitated and more photo-holes were generated for photodegradation MB. The photo-holes generation capacity of the BiOBr/Cu foam was verified by the $\bullet OH$ production. The reason was due to $\bullet OH$ was produced by photo-holes oxidation of OH^- or water molecule [39]. DMPO was employed as a probe to detect hydroxyl radicals ($\bullet OH$), and the DMPO-OH signal was identified using a quartet 1:2:2:1 model with $g = 2.0060$ as the center [40]. As shown in Fig. 5a, no peaks were found in the pure Cu foam, indicating no $\bullet OH$ generation in the pure Cu

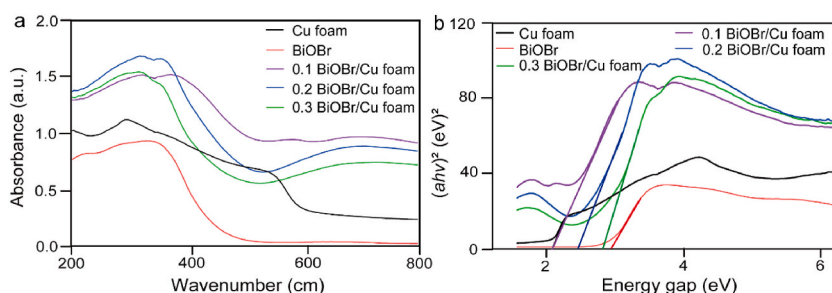


Fig. 3. UV-vis diffuse reflectance spectra and plot of $(h\nu)^2/n$ vs. energy $(h\nu)$ for the band-gap energy of BiOBr/Cu foam samples.

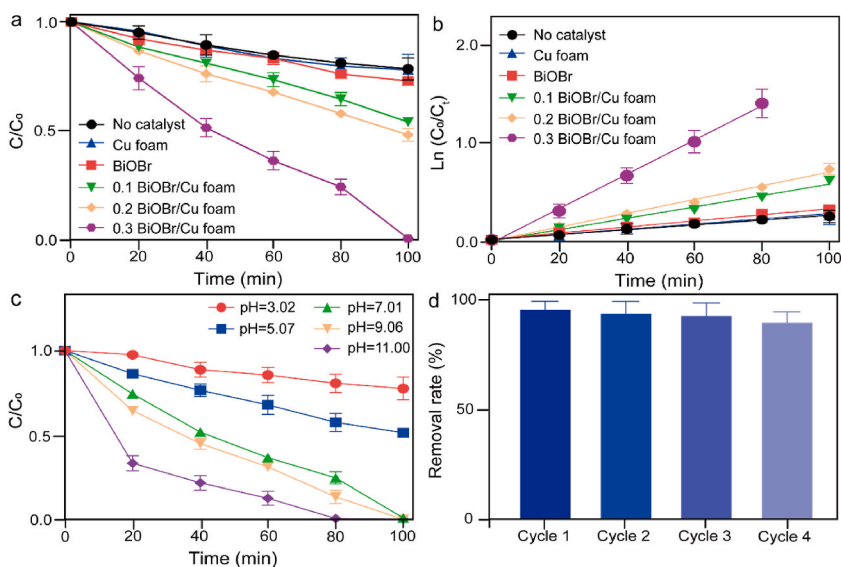


Fig. 4. (a) Photodegradation of 10 mg/L MB using BiOBr/Cu foam under solar light irradiation (pH = 7.00), (b) pseudo-first order kinetics fitting and (c) at different pH value; (d) Reusability of 0.3 BiOBr/Cu foam for 10 mg/L MB photodegradation under solar light irradiation (pH = 7.00).

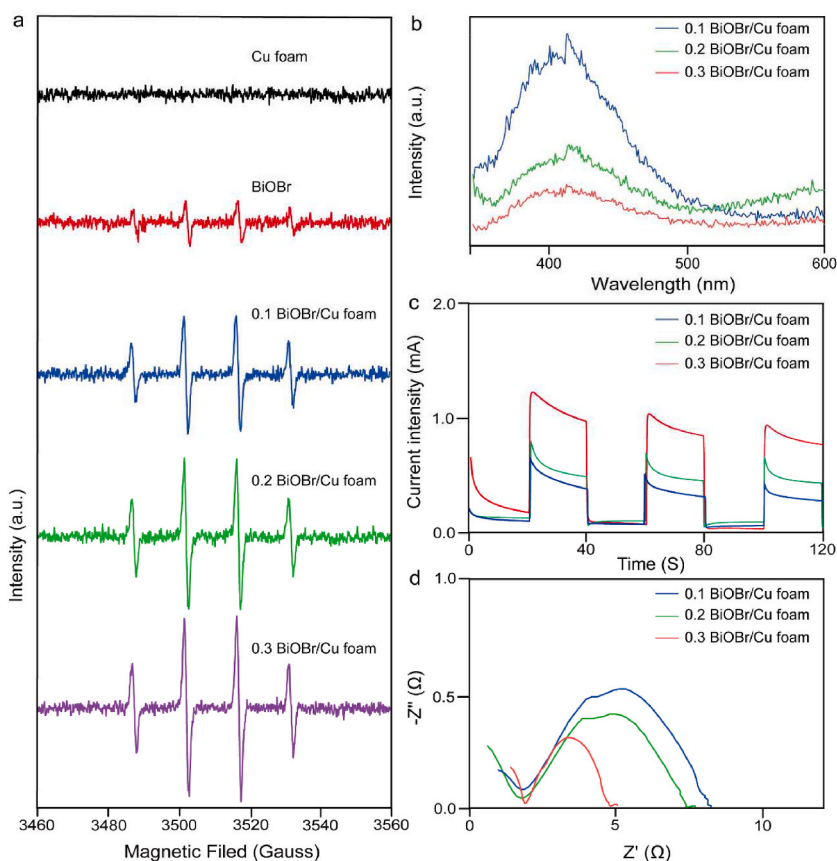


Fig. 5. (a) DMPO spin-trapping ESR spectra (DMPO-OH) of BiOBr/Cu foam under solar light irradiation; (b) photoluminescence spectra of BiOBr/Cu foam using an excitation wavelength at 320 nm; (c) photocurrent and (d) electrochemical impedance spectra of BiOBr/Cu foam under solar light irradiation. The experimental were performed in 0.5 M sodium sulfate.

foam under solar light. In contrast, the signal intensity of DMPO-OH is increased in the case of the BiOBr under solar light irradiation. Specifically, when BiOBr is loaded onto the Cu foam, the DMPO-OH signal intensity of BiOBr/Cu foam significantly surpasses that of pristine BiOBr, indicating the $\bullet\text{OH}$ generation in the BiOBr/Cu foam much more the pure Cu foam. Besides, the DMPO-OH signal intensity of 0.3 BiOBr/Cu foam was the highest among other samples. This was probably because the loading dose of BiOBr on the Cu foam was much more than that of other samples.

Furthermore, the solar light-sensitized charge separation mechanism of BiOBr/Cu foam was investigated by photoluminescence, photocurrent, and electrochemical impedance analysis. As shown in the photoluminescence spectrum (Fig. 5b), the photoluminescence emission intensity of 0.3 BiOBr/Cu foam exhibited a notable reduction in comparison to that of 0.1 BiOBr/Cu foam and 0.2 BiOBr/Cu foam, suggesting more efficient charge separation of 0.3 BiOBr/Cu foam [41]. The photocurrent analysis (Fig. 5c) showed that loading BiOBr on Cu foam had an obvious acceleration of the photogenerated current density than that of BiOBr and Cu foam, indicating coupling with BiOBr and Cu foam can promote charge separation. The maximum photocurrent was observed with the 0.3 BiOBr/Cu foam, indicating the maximum quantum yield was generated in the 0.3 BiOBr/Cu foam [42]. The electrochemical impedance spectrum (Fig. 5d) showed that the radius of the semicircle decreases in the order of Cu foam > BiOBr > 0.1 BiOBr/Cu foam > 0.2 BiOBr/Cu foam > 0.3 BiOBr/Cu foam which suggested that the interface charge transfer resistance also decreases in the same order [43]. These results suggested that Cu foam is similar to metal, acting as a scavenger of electrons in the BiOBr/Cu foam, facilitating the BiOBr charge separation and photo-induced holes generation.

3.4. Potential mechanism of MB degradation by BiOBr/Cu foam

Photo-electrons, photo-holes, and various ROS were the major impetus to degrade the organic compounds in the photocatalytic process [44]. In the MB photodegradation, various active substances play a pivotal role depending on the specific photocatalysts and reaction systems [45]. Therefore, it is necessary to further explore the mechanism of MB degradation. Scavengers for photo-electrons, photo-holes, and various ROS were added in the MB photodegradation, and the result is shown in Fig. 6. The addition of p-benzoquinone, sodium oxalate, or isopropanol considerably inhibited the MB photodegradation, indicating the essential participation of superoxide anion, photo-holes, and $\bullet\text{OH}$ in MB photodegradation. In particular, MB was almost not degraded when the scavenger of $\bullet\text{OH}$ was added, indicating $\bullet\text{OH}$ was the key active substance for MB degradation [46]. In general, in addition to the photo-holes oxidation of OH^- or water molecules, $\bullet\text{OH}$ can also come from the photodecomposition of hydrogen peroxide generated by photo-electrons reduction, resulting in the inhibition effect of MB photodegradation by adding photo-holes scavenger was lower than that by adding $\bullet\text{OH}$ scavenger [47]. Besides, the addition of potassium bromate slightly enhanced the MB photodegradation. This is probably because quenching photo-electrons can promote charge separation and photo-holes generation, and then lead to more $\bullet\text{OH}$ generation [48].

Based on the above, the potential mechanism of MB degradation by BiOBr/Cu foam was described as follows (Scheme 1): Cu foam, serving as a conductive substrate for immobilizing BiOBr, enhances the separation and reusability of the photocatalyst in the solution, thereby reducing the overall cost of the photocatalytic process. By acting as an electron scavenger in the BiOBr/Cu foam, it facilitates the transfer of photo-electrons from BiOBr valence band to BiOBr conduction band under solar light irradiation, leading to increased generation of photo-induced holes. Moreover, $\bullet\text{OH}$ can be generated, as the photo-induced holes react with OH^- or H_2O . Consequently, Methylene Blue (MB) can be rapidly degraded through the abundance of $\bullet\text{OH}$, producing CO_2 and H_2O .

4. Conclusion

In this study, the in-situ growth of BiOBr on Cu foam was employed to circumvent the typical photocatalysts drawbacks of the wide band gap, swift recombination of photo-induced electron/hole pairs, and intricate separation and recovery processes in the photocatalytic process. MB is utilized as a representative organic pollutant to assess the photodegradation performance of various doses of

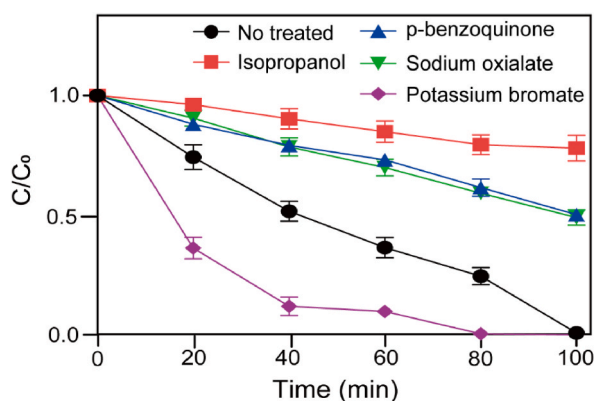
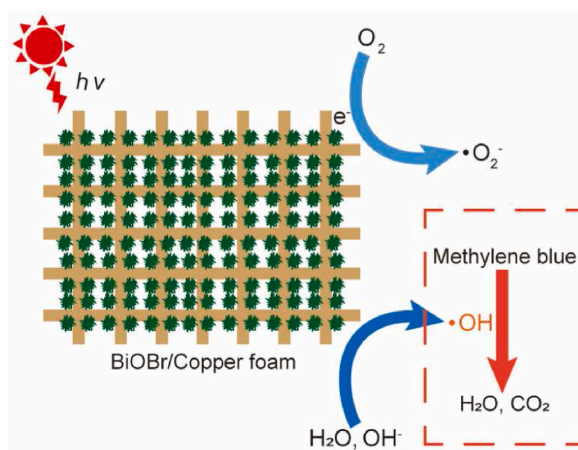


Fig. 6. Kinetics of photodegradation of 10 mg/L MB using 0.3 BiOBr/Cu foam with various quenchers under solar light irradiation (pH = 7.00).



Scheme 1. The pathway of MB photodegradation by BiOBr/Cu foam.

BiOBr on Cu foam. The results indicate that 0.3 BiOBr/Cu foam exhibits superior photocatalytic efficacy compared to other photocatalysts under solar light irradiation, while also enabling easy separation from the solution for potential reuse. Quenching assessments suggest that $\cdot OH$ play a pivotal role in MB photodegradation. The enhanced performance in MB photodegradation through BiOBr loading on Cu foam is attributed to the role of Cu foam as an electron scavenger within the BiOBr/Cu foam. These findings present a novel approach to crafting and synthesizing composite photocatalysts using conductive substrates, aiming to achieve efficient photodegradation of environmental contaminants.

CRediT authorship contribution statement

Ying Liang: Writing – original draft, Investigation, Data curation, Conceptualization. **Ting Yu:** Writing – original draft, Investigation, Data curation, Conceptualization. **Man Lang:** Investigation, Data curation. **Fengjie Chen:** Writing – review & editing, Project administration, Investigation, Funding acquisition. **Mengxi Cao:** Resources. **Bolei Chen:** Resources. **Pu Wang:** Resources. **Yong Liang:** Resources. **Yawei Wang:** Resources.

Declaration of competing interest

The authors declare that they have no known competing financial interests or personal relationships that could have influenced the work reported in this paper.

Acknowledgements

This work was supported by the State Key Laboratory of Precision Blasting, Jiangnan University (No. PBSKL2022301), the Excellent Discipline Cultivation Project by JHUN (2023XKZ028), the Hubei University Excellent Young and Middle-aged Science and Technology Innovation Team Project (No. T2021037), the Hubei Provincial Science and Technology Innovation Talent Plan project (2023DJC137), and the National Natural Science Foundation of China (Nos. 22136006, 21705057).

Appendix A. Supplementary data

Supplementary data to this article can be found online at <https://doi.org/10.1016/j.heliyon.2024.e25929>.

References

- [1] S.H. Paiman, et al., Insight into photocatalysis technology as a promising approach to tackle microplastics pollution through degradation and upcycling, *Chem. Eng. J.* 467 (2023) 143534.
- [2] K.B. Jiang, et al., Photobreeding heterojunction on semiconductor materials for enhanced photocatalysis, *Adv. Func. Mater.* (2023) 2304351.
- [3] W. Zhu, et al., AgBr nanoparticles in situ growth on 2D MoS₂ nanosheets for rapid bacteria-killing and photodisinfection, *ACS Appl. Mater. Interfaces* 11 (37) (2019) 34364–34375.
- [4] Y.-n. Zhou, et al., Solvents mediated-synthesis of 3D-BiOX (X = Cl, Br, I) microspheres for photocatalytic removal of gaseous Hg⁰ from the zinc smelting flue gas, *Fuel* 268 (2020) 117211.
- [5] J. Ni, et al., Hierarchical defect-rich flower-like BiOBr/Ag nanoparticles/ultrathin g-C₃N₄ with transfer channels plasmonic Z-scheme heterojunction photocatalyst for accelerated visible-light-driven photothermal-photocatalytic oxytetracycline degradation, *Chem. Eng. J.* 419 (2021) 129969.

- [6] C.-J. Chang, et al., Enhanced visible-light-driven photocatalytic degradation by metal wire-mesh supported Ag/flower-like Bi₂WO₆ photocatalysts, *J. Alloys Compd.* 813 (2020) 152186.
- [7] F. Khurshid, M. Jeyavelan, S. Nagarajan, Photocatalytic dye degradation by graphene oxide doped transition metal catalysts, *Synt. Met.* 278 (2021) 116832.
- [8] J. Zhao, et al., BiOBr nanoflakes with engineered thickness for boosted photodegradation of RhB under visible light irradiation, *J. Alloys Compd.* 947 (2023) 169613.
- [9] R. Jiang, et al., The bonding and intercalation efficacy of polyethyleneimine enhanced BiOBr semiconductor-organic framework degradation and detoxification of bisphenol AF, *Sep. Purif. Technol.* 320 (2023) 124134.
- [10] Y. Wang, Y. Long, D. Zhang, Facile in situ growth of high strong BiOI network films on metal wire meshes with photocatalytic activity, *ACS Sustain. Chem. Eng.* 5 (3) (2017) 2454–2462.
- [11] D. He, et al., Photo-activated direct catalytic oxidation of gaseous benzene with a Cu-connected serial heterojunction array of Co₃O₄/Cu_xO/foam Cu assembled via layer upon layer oxidation, *Small* 19 (29) (2023) 202207114.
- [12] F. Cao, T. Wang, X. Ji, Enhanced visible photocatalytic activity of tree-like ZnO/CuO nanostructure on Cu foam, *Appl. Surf. Sci.* 471 (2019) 417–424.
- [13] X. Zhong, et al., In-situ growth of COF on BiOBr 2D material with excellent visible-light-responsive activity for U(VI) photocatalytic reduction, *Sep. Purif. Technol.* 279 (2021) 119627.
- [14] R.R. Siti Fatimah, D.F. Al Husaeni, A.B. Dani Nandiyanto, How to calculate crystallite size from X-ray diffraction (XRD) using scherrer method, *ASEAN J. Sci. Eng.* 2 (1) (2022) 65–76.
- [15] Q. Fan, et al., Regulating the stability and bandgap structure of BiOBr during thermo-transformation via La doping, *Appl. Surf. Sci.* 481 (2019) 564–575.
- [16] H.-P. Jiao, et al., One-pot synthesis of heterostructured Bi₂S₃/BiOBr microspheres with highly efficient visible light photocatalytic performance, *RSC Adv.* 5 (21) (2015) 16239–16249.
- [17] J.M. Mora-Hernandez, et al., An enhanced photo(electro)catalytic CO₂ reduction onto advanced BiOX (X = Cl, Br, I) semiconductors and the BiOI–PdCu composite, *Heliyon* 9 (10) (2023) e20605.
- [18] M.d.C. Rangel, et al., Selecting catalysts for pyrolysis of lignocellulosic biomass, *Biomass* 3 (1) (2023) 31–63.
- [19] V.H. Luan, et al., Synthesis of a highly conductive and large surface area graphene oxide hydrogel and its use in a supercapacitor, *J. Mater. Chem. A* 1 (2) (2013) 208–211.
- [20] F. Cao, et al., An in situ bi-decorated biobr photocatalyst for synchronously treating multiple antibiotics in water, *Nanoscale Adv.* 1 (3) (2019) 1124–1129.
- [21] J. Zhao, et al., Flexible cotton fabrics/PDA/BiOBr composite photocatalyst using bioinspired polydopamine as electron transfer mediators for dye degradation and Cr(VI) reduction under visible light, *Colloids Surf. A Physicochem. Eng. Asp.* 593 (2020) 124623.
- [22] Y. Zhu, et al., ZnOCu₂O/g-C₃N₄ heterojunctions with enhanced photocatalytic activity for removal of hazardous antibiotics, *Heliyon* 8 (12) (2022) e12644.
- [23] S.R. Zhu, et al., Hierarchical core-shell SiO₂@PDA@BiOBr microspheres with enhanced visible-light-driven photocatalytic performance, *Dalton Trans.* 46 (34) (2017) 11451–11458.
- [24] J. Hongxia, et al., A new double Z-scheme TiO₂/ZnO-g-C₃N₄ nanocomposite with enhanced photodegradation efficiency for Rhodamine B under sunlight, *Environ. Prog. Sustain. Energy* 42 (1) (2022) 13968.
- [25] Y. Zheng, et al., A conjugated composite of α-Fe₂O₃ and biobr with enhanced visible-light-induced photocatalytic activity, *J. Mol. Catal. Chem.* 421 (2016) 16–28.
- [26] I. Mehmood, et al., Mn doped CdS passivated CuInSe₂ quantum dot sensitized solar cells with remarkably enhanced photovoltaic efficiency, *RSC Adv.* 7 (53) (2017) 33106–33112.
- [27] T.D. Dao, et al., Plasmon-mediated photocatalytic activity of wet-chemically prepared ZnO nanowire arrays, *Phys. Chem. Chem. Phys.* 17 (11) (2015) 7395–7403.
- [28] S. Argote-Fuentes, et al., Photoelectrocatalytic degradation of Congo red dye with activated hydrotalcites and copper anode, *Catalysts* 11 (2) (2021) 211.
- [29] Y. Guo, et al., Effect of pH on the catalytic degradation of Rhodamine B by synthesized CdS/g-C₃N₄/Cu_xO composites, *ACS Omega* 6 (12) (2021) 8119–8130.
- [30] J.-H. Shen, et al., Mechanistic insights into hydroxyl radical formation of Cu-doped ZnO/g-C₃N₄ composite photocatalysis for enhanced degradation of ciprofloxacin under visible light: efficiency, kinetics, products identification and toxicity evaluation, *J. Environ. Chem. Eng.* 10 (2) (2022) 107352.
- [31] L. Luo, et al., Recent advances in heterogeneous photo-driven oxidation of organic molecules by reactive oxygen species, *ChemSusChem* 13 (19) (2020) 5173–5184.
- [32] T.T. Minh, et al., Synthesis of porous octahedral ZnO/CuO composites from Zn/Cu-based MOF-199 and their applications in visible-light-driven photocatalytic degradation of dyes, *J. Nanomater.* 2019 (2019) 1–16.
- [33] M. Kaur1, Imine-decorated copper-based metal-organic framework for the photodegradation of methylene blue, *J. Fluoresc.* 2023 (2023), 03346-5.
- [34] M.F.C. Ling, K.C. Hui, N.S. Sambudi, Modification of TiO₂ with clam-shell powder for photodegradation of methylene blue, *J. Sol. Gel Sci. Technol.* 102 (2) (2022) 412–421.
- [35] D. Zhang, et al., The photodegradation of methylene blue in water with PVDF/GO/ZnO composite membrane, *Mater. Sci. Eng. C* 96 (2019) 684–692.
- [36] A.A. Shah, et al., Facile synthesis of copper doped ZnO nanorods for the efficient photo degradation of methylene blue and methyl orange, *Ceram. Int.* 46 (8) (2020) 9997–10005.
- [37] R. Yanagi, et al., Charge separation in photocatalysts: mechanisms, physical parameters, and design principles, *ACS Energy Lett.* 7 (1) (2021) 432–452.
- [38] C.H. Hak, et al., M/g-C₃N₄ (M=Ag, Au, and Pd) composite: synthesis via sunlight photodeposition and application towards the degradation of bisphenol A, *Environ. Sci. Pollut. Res.* 25 (25) (2018) 25401–25412.
- [39] C. Yin, et al., Detection of hydroxyl radicals in sonoelectrochemical system, *Microchem. J.* 144 (2019) 369–376.
- [40] K.P. Madden, H. Taniguchi, The role of the DMPO-hydrated electron spin adduct in DMPO-radical dotOH spin trapping, *Free Radical. Bio. Med.* 30 (12) (2001) 1374–1380.
- [41] X. Jin, et al., Influences of synthetic conditions on the photocatalytic performance of ZnS/graphene composites, *J. Alloys Compd.* 780 (2019) 299–305.
- [42] A. Behera, et al., Facile synthesis of ZnFe₂O₄@RGO nanocomposites towards photocatalytic ciprofloxacin degradation and H₂ energy production, *J. Colloid Interface Sci.* 556 (2019) 667–679.
- [43] C. Lv, et al., Oxygen-Induced Bi⁵⁺-self-doped Bi₄V₂O₁₁ with a p–n homojunction toward promoting the photocatalytic performance, *ACS Appl. Mater. Interfaces* 9 (28) (2017) 23748–23755.
- [44] L. Wang, et al., Photodegradation of clindamycin by the dissolved black carbon is simultaneously regulated by ROS generation and the binding effect, *Water Res.* 233 (2023) 119784.
- [45] G.S. Das, et al., Biomass-derived carbon quantum dots for visible-light-induced photocatalysis and label-free detection of Fe(III) and ascorbic acid, *Sci. Rep.* 9 (1) (2019) 15084.
- [46] S. Xin, et al., Enhanced heterogeneous photo-fenton-like degradation of tetracycline over CuFeO₂/biochar catalyst through accelerating electron transfer under visible light, *J. Environ. Manag.* 285 (2021) 112093.
- [47] Y. Ou, et al., Photoenhanced oxidation of nC₆₀ in water: exploring H₂O₂ and hydroxyl radical based reactions, *Chem. Eng. J.* 360 (2019) 665–672.
- [48] Q. Hu, et al., Ultrathin graphitic carbon nitride modified PbBiO₂Cl microspheres with accelerating interfacial charge transfer for the photodegradation of organic contaminants, *Colloids Surf. A Physicochem. Eng. Asp.* 582 (2019) 123804.